

Flow Matching is Adaptive to Manifold Structures

Shivam Kumar¹, Yixin Wang², and Lizhen Lin³

¹Booth School of Business, University of Chicago

²Department of Statistics, University of Michigan

³Department of Mathematics, University of Maryland, College Park

Abstract

Flow matching has emerged as a simulation-free alternative to diffusion-based generative modeling, producing samples by solving an ODE whose time-dependent velocity field is learned along an interpolation between a simple source distribution (e.g., a standard normal) and a target data distribution. Flow-based methods often exhibit greater training stability and have achieved strong empirical performance in high-dimensional settings where data concentrate near a low-dimensional manifold, such as text-to-image synthesis, video generation, and molecular structure generation. Despite this success, existing theoretical analyses of flow matching assume target distributions with smooth, full-dimensional densities, leaving its effectiveness in manifold-supported settings largely unexplained. To this end, we theoretically analyze flow matching with linear interpolation when the target distribution is supported on a smooth manifold. We establish a non-asymptotic convergence guarantee for the learned velocity field, and then propagate this estimation error through the ODE to obtain statistical consistency of the implicit density estimator induced by the flow-matching objective. The resulting convergence rate is near minimax-optimal, depends only on the intrinsic dimension, and reflects the smoothness of both the manifold and the target distribution. Together, these results provide a principled explanation for how flow matching adapts to intrinsic data geometry and circumvents the curse of dimensionality.

1 Introduction

Flow matching (Albergo et al., 2023; Liu et al., 2022; Albergo and Vanden-Eijnden, 2022; Lipman et al., 2022) has recently emerged as a simulation-free alternative to diffusion-based generative modeling, producing samples by solving an ordinary differential equation (ODE) whose time-dependent velocity field transports probability mass between distributions. Unlike diffusion models, which rely on stochastic perturbations and reverse-time SDE simulation, flow matching learns a deterministic transport map along a prescribed interpolation between a simple source distribution (e.g., a standard normal) and a target data distribution.

The deterministic formulation of flow matching yields favorable computational properties, including stable training, flexible discretization at sampling time, and compatibility with modern continuous normalizing flow (CNF) architectures (Lipman et al., 2022; Liu et al., 2022). Empirically, flow matching has achieved strong performance in high-dimensional generative tasks such as text-to-image synthesis, video generation, and molecular structure modeling, where data are known to concentrate near low-dimensional manifolds (Bose et al., 2023; Graham and Purver, 2024; Esser et al., 2024; Ma et al., 2024).

Despite this empirical success, theoretical foundations of flow matching remain limited. Existing analyses typically assume that the target distribution admits a smooth, full-dimensional density with respect to Lebesgue measure. This assumption is misaligned with many modern applications, where the data distribution is intrinsically low-dimensional and supported on or near a smooth manifold embedded in a high-dimensional ambient space. As a result, current theory does not explain why flow matching avoids the curse of dimensionality in practice, nor how its performance depends on intrinsic geometric structure.

To formalize this setting, we observe an i.i.d. dataset $\mathcal{D}_1 = \{X_{1,j}\}_{j=1}^n$, where $X_1 \sim \pi_1$ is drawn from a target distribution supported on a d -dimensional manifold \mathcal{M} embedded in the ambient space \mathbb{R}^D . Flow matching constructs a continuous probability path $(X_t)_{t \in [0,1]}$ connecting a simple reference distribution π_0 , from which sampling is straightforward, to the target distribution π_1 . This path is governed by a time-dependent vector field $v^* : \mathbb{R}^D \times [0, 1] \rightarrow \mathbb{R}^D$, and the state evolves according to the transport ODE

$$\frac{dX_t}{dt} = v^*(X_t, t), \quad X_0 \sim \pi_0 = \mathbb{N}(\mathbf{0}, \mathbb{I}_D), \quad X_1 \sim \pi_1. \quad (1)$$

The goal of flow matching is to estimate the velocity field v^* from data. Once an estimate \hat{v} is obtained, approximate samples of π_1 are generated by drawing $X_0 \sim \pi_0$ and numerically integrating the ODE (1) forward in time from $t = 0$ to $t \approx 1$.

When π_1 is supported on a manifold, it is singular with respect to Lebesgue measure, so the appropriate statistical target is the pushforward distribution induced by the learned dynamics. We therefore treat $\hat{\pi}_{1-t}$ as an implicit estimator of π_1 (see (10)), and derive non-asymptotic convergence bounds that are intrinsically nonparametric and governed by the manifold dimension.

We provide a theoretical analysis of distribution estimation using flow matching with linear interpolation, in the manifold-supported setting. Our analysis yields non-asymptotic convergence guarantees for estimating the velocity field and propagate this estimation error through the transport ODE to obtain statistical consistency of the implicit density estimator. The resulting convergence rates are near minimax-optimal, depend only on the intrinsic dimension d , and capture the smoothness of both the manifold and the target distribution.

Together, these results provide a principled explanation for why flow matching can adapt to intrinsic geometry and mitigate the curse of dimensionality.

1.1 List of contributions

We briefly summarize the main contributions of this paper as follows.

- We provide a non-asymptotic error analysis of flow matching with linear interpolation when the target distribution is supported on a low-dimensional manifold embedded in \mathbb{R}^D . The resulting rate is near-minimax optimal and depends only on structural properties of the target distribution.
- Our convergence guarantees show that flow matching adapts to the manifold structure of the data: the statistical complexity is governed by the intrinsic dimension rather than the ambient dimension. To the best of our knowledge, this is the first work to develop a finite-sample error analysis of flow matching in the manifold-supported setting.
- We establish consistency rates for estimating the velocity field $v^*(\mathbf{x}, t)$. In particular, the estimator attains fast convergence for times bounded away from $t = 1$, while the rate deteriorates as $t \rightarrow 1$ due to the singular behavior of the linear-path velocity field.

1.2 Other relevant literature

In the context of manifold-based generative modeling, our work is most closely related to [Tang and Yang \(2024\)](#); [Azangulov et al. \(2024\)](#), which develop diffusion-model theory showing how diffusion adapts to data geometry. While conceptually aligned, our setting differs in a fundamental way: flow matching is a simulation-free alternative to diffusion, with a distinct training objective and proof strategy. Accordingly, our technical approach is closer in spirit to the tools used in [Gao et al. \(2024a\)](#) and [Kunkel \(2025b\)](#) to derive non-asymptotic convergence guarantees. The work of [Chen and Lipman \(2023\)](#) studies an empirical form of flow matching on manifolds in a different regime, where both the learned velocity field and the induced flow remain entirely supported on the manifold. In contrast, our analysis allows the dynamics to evolve in the ambient space, while still adapting to the intrinsic geometry through the target distribution.

A few recent works study error analysis and convergence rates for flow matching ([Gao et al., 2024b](#); [Marzouk et al., 2024](#); [Fukumizu et al., 2024](#); [Kunkel, 2025a](#); [Zhou and Liu, 2025](#)). However, these results focus on targets supported in the full ambient space and do not explicitly exploit manifold geometry. In particular, the rates in [Gao et al. \(2024b\)](#) and [Zhou and Liu \(2025\)](#) are not near minimax-optimal.

Beyond statistical error analysis, flow matching has also been studied from several complementary perspectives, including deterministic straightening ([Liu et al., 2022](#); [Bansal et al., 2024](#); [Kornilov et al., 2024](#)), fast sampling ([Hu et al., 2024a](#); [Gui et al., 2025](#)), latent structures ([Dao et al., 2023](#); [Hu et al., 2024b](#)), and discrete analogues ([Davis et al., 2024](#); [Gat et al., 2024](#); [Su et al., 2025](#); [Cheng et al., 2025](#)), among others.

1.3 Notations

We write \mathbb{N} for the positive integers and \mathbb{R}^m for m -dimensional Euclidean space. For $r > 0$ and $\mathbf{x} \in \mathbb{R}^D$, $\mathbb{B}_r(\mathbf{x})$ denotes the (closed) Euclidean ball of radius r centered at \mathbf{x} . We use $a \vee b := \max\{a, b\}$ and $a \wedge b := \min\{a, b\}$. Scalars are denoted by lower-case letters, vectors by bold lower-case (e.g. \mathbf{x}), and matrices by bold upper-case (e.g. \mathbf{A}). We write $\mathbb{I}_D \in \mathbb{R}^{D \times D}$ for the identity matrix. For $p \in [1, \infty]$, $\|\cdot\|_p$ denotes the usual ℓ_p norm (and the induced operator norm for matrices). For a function f , $\|f\|_\infty := \sup_x |f(x)|$. The indicator of an event A is denoted by $\mathbb{1}_A$. For sequences $a_n, b_n \geq 0$, we write $a_n \lesssim b_n$ if there exists an absolute constant $C > 0$ (independent of n) such that $a_n \leq Cb_n$; similarly $a_n \gtrsim b_n$ and $a_n \asymp b_n$. We use $\mathcal{O}(\cdot)$ and $o(\cdot)$ in the standard sense. The indicator function of an event A is $\mathbb{1}_A$. We write $\mathbf{N}(\mathbf{m}, \Sigma)$ for a Gaussian distribution with mean \mathbf{m} and covariance Σ . We denote probability and expectation by \mathbb{P} and \mathbb{E} , and conditional expectation by $\mathbb{E}[\cdot | \cdot]$. For two probability density μ, ν on \mathbb{R}^D with finite p -th moments, $W_p(\mu, \nu)$ denotes the p -Wasserstein distance. For a multi-index $\alpha = (\alpha_1, \dots, \alpha_d) \in \mathbb{N}^d$, let $|\alpha| := \sum_{j=1}^d \alpha_j$ and $\partial^\alpha := \partial_1^{\alpha_1} \dots \partial_d^{\alpha_d}$. For $\beta > 0$ and a domain $D \subset \mathbb{R}^d$, the β -Hölder class $\mathcal{H}_d^\beta(D, K)$ is

$$\mathcal{H}_d^\beta(D, K) := \left\{ f : D \rightarrow \mathbb{R} : \sum_{|\alpha| < \beta} \|\partial^\alpha f\|_\infty + \sum_{|\alpha| = \lfloor \beta \rfloor} \sup_{\substack{\mathbf{u}_1, \mathbf{u}_2 \in D \\ \mathbf{u}_1 \neq \mathbf{u}_2}} \frac{|\partial^\alpha f(\mathbf{u}_1) - \partial^\alpha f(\mathbf{u}_2)|}{\|\mathbf{u}_1 - \mathbf{u}_2\|_\infty^{\beta - \lfloor \beta \rfloor}} \leq K \right\}.$$

A map $f : \mathbb{R}^D \rightarrow \mathbb{R}^m$ is L -Lipschitz if $\|f(\mathbf{x}) - f(\mathbf{y})\|_\infty \leq L\|\mathbf{x} - \mathbf{y}\|_\infty$ for all \mathbf{x}, \mathbf{y} .

2 Flow matching

The evolution of the probability density $\pi_t(\mathbf{x})$ associated with a flow $(X_t)_{t \in [0,1]}$ is governed by the continuity (or transport) equation:

$$\begin{aligned} \partial_t \pi_t(\mathbf{x}) + \nabla \cdot (\pi_t(\mathbf{x}) v_*(\mathbf{x}, t)) &= 0, \\ \pi_0(\mathbf{x}) &= (\sqrt{2\pi})^{-1} \exp(-|\mathbf{x}|_2^2/2), \quad \pi_1(\mathbf{x}). \end{aligned} \tag{2}$$

A popular strategy is to construct a coupling (X_0, X_1) and define an interpolation $X_t = F(X_0, X_1, t)$ for $t \in [0, 1]$. The resulting curve $(X_t)_{t \in [0,1]}$ induces a time-dependent velocity field. Under appropriate regularity assumptions on the interpolation path, it is known (Albergo et al., 2023, Theorem 6) that the velocity field v^* is given by the conditional expectation

$$v^*(t, \mathbf{x}) = \mathbb{E} \left[\dot{X}_t \mid X_t = \mathbf{x} \right].$$

Linear interpolation. Throughout this paper we focus on flow matching with the *linear* interpolation path

$$X_t := tX_1 + (1-t)X_0, \quad t \in [0, 1], \tag{3}$$

where $X_0 \sim \pi_0 = \mathcal{N}(\mathbf{0}, \mathbb{I}_D)$ and $X_1 \sim \pi_1$ (with X_0 independent of X_1). Since $\dot{X}_t = X_1 - X_0$, the induced velocity field admits the conditional-expectation representation

$$\begin{aligned} v^*(\mathbf{x}, t) &= \mathbb{E} [X_1 - X_0 \mid X_t = \mathbf{x}] \\ &= \frac{1}{1-t} \left[\frac{\int_{\mathbf{y} \in \mathcal{M}} \mathbf{y} \pi_1(\mathbf{y}) e^{-\frac{|\mathbf{x}-t\mathbf{y}|_2^2}{2(1-t)^2}} d\mathbf{y}}{\int_{\mathbf{y} \in \mathcal{M}} \pi_1(\mathbf{y}) e^{-\frac{|\mathbf{x}-t\mathbf{y}|_2^2}{2(1-t)^2}} d\mathbf{y}} - \mathbf{x} \right], \end{aligned} \tag{4}$$

with a short derivation deferred to Section C.1. The derivation uses the linearity of the flow (3) so that the instantaneous change is independent of time apart from the interpolation weights. Linear-interpolation flow matching has demonstrated strong empirical performance in large-scale generative modeling (Liu et al., 2022; Tong et al., 2023; Esser et al., 2024).

Optimization. Learning the velocity field in this setting amounts to formulating an optimization problem whose solution recovers v^* as in (4). Consider the population risk functional

$$\min_u \mathcal{L}(u) \quad \text{where} \quad \mathcal{L}(u) := \int_0^1 \mathbb{E} \left[\|u(X_t, t) - \dot{X}_t\|_2^2 \right] dt. \tag{5}$$

In Lemma 5, we show that v^* is a minimizer of \mathcal{L} , i.e., $v^* \in \arg \min_u \mathcal{L}(u)$.

2.1 Neural network class

A neural network with $L \in \mathbb{N}$ layers, $n_l \in \mathbb{N}$ many nodes at the l -th hidden layer for $l = 1, \dots, L$, input of dimension n_0 , output of dimension n_{L+1} and nonlinear activation function $\text{ReLU } \rho : \mathbb{R} \rightarrow \mathbb{R}$ is expressed as

$$\mathbf{N}_\rho(\mathbf{x}|\boldsymbol{\theta}) := \mathbf{A}_{L+1} \circ \sigma_L \circ \mathbf{A}_L \circ \dots \circ \sigma_1 \circ \mathbf{A}_1(\mathbf{x}), \tag{6}$$

where $A_l : \mathbb{R}^{n_{l-1}} \rightarrow \mathbb{R}^{n_l}$ is an affine linear map defined by $A_l(\mathbf{x}) = \mathbf{W}_l \mathbf{x} + \mathbf{b}_l$ for given $n_l \times n_{l-1}$ dimensional weight matrix \mathbf{W}_l and n_l dimensional bias vector \mathbf{b}_l and $\sigma_l : \mathbb{R}^{n_l} \rightarrow \mathbb{R}^{n_l}$ is an element-wise nonlinear activation map defined by $\sigma_l(\mathbf{z}) := (\sigma(z_1), \dots, \sigma(z_{n_l}))^\top$. We use $\boldsymbol{\theta}$ to denote the set of all weight matrices and bias vectors $\boldsymbol{\theta} := ((\mathbf{W}_1, \mathbf{b}_1), (\mathbf{W}_2, \mathbf{b}_2), \dots, (\mathbf{W}_{L+1}, \mathbf{b}_{L+1}))$.

Following a standard convention, we say that $L(\boldsymbol{\theta})$ is the depth of the deep neural network and $n_{\max}(\boldsymbol{\theta})$ is the width. We let $|\boldsymbol{\theta}|_0$ be the number of nonzero elements of $\boldsymbol{\theta}$, i.e.,

$$|\boldsymbol{\theta}|_0 := \sum_{l=1}^{L+1} \left(|\text{vec}(\mathbf{W}_l)|_0 + |\mathbf{b}_l|_0 \right),$$

where $\text{vec}(\mathbf{W}_l)$ transforms the matrix \mathbf{W}_l into the corresponding vector by concatenating the column vectors. We call $|\boldsymbol{\theta}|_0$ sparsity of the deep neural network. Let $|\boldsymbol{\theta}|_\infty$ be the largest absolute value of elements of $\boldsymbol{\theta}$, i.e.,

$$|\boldsymbol{\theta}|_\infty := \max \left\{ \max_{1 \leq l \leq L+1} |\text{vec}(\mathbf{W}_l)|_\infty, \max_{1 \leq l \leq L+1} |\mathbf{b}_l|_\infty \right\}.$$

We denote by $\Theta_{\mathbf{d}, \mathbf{o}}(L, W, S, B)$ the set of network parameters with depth L , width W , sparsity S , absolute value B , input dimension \mathbf{d} and output dimension \mathbf{o} , that is,

$$\begin{aligned} \Theta_{\mathbf{d}, \mathbf{o}}(L, W, S, B) := & \left\{ \boldsymbol{\theta} : L(\boldsymbol{\theta}) \leq L, n_{\max}(\boldsymbol{\theta}) \leq W, \right. \\ & \left. |\boldsymbol{\theta}|_0 \leq S, |\boldsymbol{\theta}|_\infty \leq B, \text{in}(\boldsymbol{\theta}) = \mathbf{d}, \text{out}(\boldsymbol{\theta}) = \mathbf{o} \right\}. \end{aligned} \quad (7)$$

2.2 Estimation and sampling

Denote by $\mathcal{D} := \mathcal{D}_1 \cup \mathcal{D}_0$ the full collection of samples used for training, where $\mathcal{D}_1 = \{X_{1,j}\}_{j=1}^n$ consists of i.i.d. observations $X_{1,j} \sim \boldsymbol{\pi}_1$, and $\mathcal{D}_0 = \{X_{0,j}\}_{j=1}^n$ consists of i.i.d. samples generated from $\boldsymbol{\pi}_0$ (since $\boldsymbol{\pi}_0$ is known) and are independent of \mathcal{D}_1 .

Let $\{t_k\}_{k=0}^K$ be a strictly *decreasing* time grid with $t_0 = 1$ and $t_K = \underline{t} > 0$. For each $j \in [n]$ and $t \in [0, 1]$, denote the linear interpolation $X_{t,j} = tX_{1,j} + (1-t)X_{0,j}$. We estimate the velocity field by empirical risk minimization:

$$\begin{aligned} \hat{v} & \in \arg \min_{u \in \mathcal{U}} \hat{\mathcal{L}}(u), \\ \hat{\mathcal{L}}(u) & := \frac{1}{n} \sum_{j=1}^n \int_0^{1-\underline{t}} \|u(X_{t,j}, t) - (X_{1,j} - X_{0,j})\|_2^2 dt. \end{aligned} \quad (8)$$

We take \mathcal{U} to be the class of deep neural networks

$$\begin{aligned} \mathcal{U} = & \left\{ u = \sum_{k=1}^K u_k(\mathbf{x}, t) \cdot \mathbb{1}_{\{1-t_{k-1} \leq t < 1-t_k\}} : \right. \\ & \left. u_k(\mathbf{x}, t) = N_\rho(\mathbf{x}, t | \boldsymbol{\theta}_k), \boldsymbol{\theta}_k \in \Theta_{\mathbf{d}, \mathbf{d}}(L_k, W_k, S_k, B_k) \right\}. \end{aligned} \quad (9)$$

Each $u \in \mathcal{U}$ is assumed to satisfy the following uniform constraints for all $t \in [0, 1 - \bar{t}]$

$$\|u(\cdot, t)\|_\infty \lesssim \frac{\sqrt{\log(n)}}{1-t}, \quad u(\cdot, t) \text{ is } \frac{C_{\text{Lip}}}{(1-t)^{1-\xi}} \text{ - Lipschitz,}$$

$t \mapsto u(\mathbf{x}, t)$ is continuous, for some constant $C_{\text{Lip}} > 0$. These constraints hold for the true velocity field v^* , as shown in the next section, and are therefore not merely artifacts of our analysis. They ensure that the candidate functions adhere to the desired regularity conditions. Once the velocity field is estimated, the flow-matching sampler is defined by the neural ODE

$$\frac{d\hat{X}_t}{dt} = \hat{v}(\hat{X}_t, t), \quad \hat{X}_0 \sim \pi_0, \quad t \in [0, 1 - \underline{t}]. \quad (10)$$

Since π_0 is easy to sample from, we generate samples by drawing $\hat{X}_0 \sim \pi_0$ and pushing them forward through (10) using a numerical ODE solver. In what follows, we study the statistical consistency of \hat{v} and of the induced pushforward density $\hat{\pi}_{1-\underline{t}}$ of $\hat{X}_{1-\underline{t}}$.

Regularity. A standard sufficient condition for existence and uniqueness of solutions to the ODE (1) is given by the Picard-Lindelöf theorem. In particular, suppose the velocity field $v_* : \mathbb{R}^D \times [0, 1) \rightarrow \mathbb{R}^D$ satisfies:

- **(Local) Lipschitz continuity in \mathbf{x} :** for each $t \in [0, 1)$ there exists $L > 0$ such that for all x, y and for every $t \in [0, 1]$,

$$|v^*(\mathbf{x}, t) - v^*(\mathbf{y}, t)|_\infty \leq L|\mathbf{x} - \mathbf{y}|_\infty;$$

- **Continuity in t :** The map $t \mapsto v_*(\mathbf{x}, t)$ is continuous for every fixed x ;

then there exists a unique solution X_t to (1) (see, e.g., [Coddington and Levinson \(1955\)](#)). Alternatively, under the weaker Carathéodory conditions, where $v_*(t, \mathbf{x})$ is measurable in t and locally Lipschitz in \mathbf{x} , one can still guarantee the existence (although uniqueness may fail) of solutions.

Note that for a solution to exist, the minimizer must exhibit well-behaved properties—specifically, it should be Lipschitz in space and continuous in time. We enforce these properties by restricting the search space \mathcal{U} , ensuring that the candidate functions adhere to the desired regularity conditions.

3 Theoretical results

In this section, we state our main statistical consistency results for velocity-field estimation, which in turn yield error bounds for implicit density estimation via flow matching.

We work in an ambient space \mathbb{R}^D , while the data concentrate on a d -dimensional embedded manifold $\mathcal{M} \subset \mathbb{R}^D$ with $d \ll D$. For $\mathbf{y} \in \mathcal{M}$, let $T_{\mathbf{y}}(\mathcal{M}) \subset \mathbb{R}^D$ denote the tangent space at \mathbf{y} , and let $\text{Proj}_{T_{\mathbf{y}}(\mathcal{M})}$ be the orthogonal projection onto $T_{\mathbf{y}}(\mathcal{M})$. We write $\text{Vol}_{\mathcal{M}}$ for the d -dimensional volume measure on \mathcal{M} induced by the embedding. Whenever we refer to a “density” π_1 on \mathcal{M} , it is understood as a Radon–Nikodym derivative with respect to $\text{Vol}_{\mathcal{M}}$.

Smooth manifold. We quantify the regularity of \mathcal{M} via local charts induced by tangent projections. Fix $\beta > 0$. We say that \mathcal{M} is β -smooth if there exist constants $r_0 > 0$ and $L > 0$ such that for every $\mathbf{y} \in \mathcal{M}$, the tangent-projection map

$$\Phi_{\mathbf{y}} : \mathcal{M} \rightarrow \mathbb{T}_{\mathbf{y}}(\mathcal{M}), \quad \Phi_{\mathbf{y}}(\mathbf{x}) := \text{Proj}_{\mathbb{T}_{\mathbf{y}}(\mathcal{M})}(\mathbf{x} - \mathbf{y}),$$

is a local diffeomorphism in a neighborhood of \mathbf{y} , with inverse chart $\Psi_{\mathbf{y}}$ defined on $\mathbb{B}_{r_0}(\mathbf{0}_{\mathbb{D}}) \cap \mathbb{T}_{\mathbf{y}}(\mathcal{M})$. Moreover, the inverse chart $\Psi_{\mathbf{y}}$ is β -Hölder smooth with Hölder norm bounded by L , uniformly over $\mathbf{y} \in \mathcal{M}$.

Assumption 1. *The target distribution admits a density π_1 (with respect to the d -dimensional volume measure on \mathcal{M}) supported on a d -dimensional manifold $\mathcal{M} \subset [-C_{\mathcal{M}}, C_{\mathcal{M}}]^{\mathbb{D}}$ embedded in $\mathbb{R}^{\mathbb{D}}$. The manifold \mathcal{M} is compact and without boundary. Moreover, \mathcal{M} is β -smooth for some $\beta \geq 2$, and has reach bounded below by a positive constant.*

Assumption 2. *The density π_1 relative to the volume measure of \mathcal{M} is α -Hölder smooth with $\alpha \in [0, \beta - 1]$, and is uniformly bounded away from zero on \mathcal{M} .*

Assumption 3. *There exists a small constant $\xi \in (0, 1)$, and $L_{\star} > 0$ such that $\|\frac{\partial}{\partial \mathbf{x}} v_{\star}(t, \mathbf{x})\|_{\text{op}} \leq \frac{L_{\star}}{(1-t)^{1-\xi}}$.*

Assumption 1 formalizes the low intrinsic-dimensional structure of the target distribution. The β -smoothness controls the regularity of \mathcal{M} (e.g., via local chart/projection representations), while the positive reach ensures the associated local projection maps are well-defined in a tubular neighborhood of \mathcal{M} . Assumption 2 enforces both smoothness and non-degeneracy of the target distribution along \mathcal{M} . The restriction $\alpha \leq \beta - 1$ aligns the regularity of π_1 with the geometric smoothness of \mathcal{M} , ensuring that the density is well-defined and stable under local projection representations. Similar assumptions are standard in manifold-based analyses of generative modeling; see, e.g., [Tang and Yang \(2024\)](#) and [Azangulov et al. \(2024\)](#). Assumption 3 is primarily technical: it provides the stability needed to utilize Theorem 3 and transfer velocity-field estimation rates to density error bounds efficiently. In the absence of such a condition, existing analyses can incur a worse dependence on the terminal time, scaling as $(1-t)^{-3}$ ([Gao et al., 2024b](#); [Zhou and Liu, 2025](#)). Similar Lipschitz-in-space assumptions (with time-dependent constants) have also been adopted in the ambient-space setting without manifold structure ([Fukumizu et al., 2024](#)).

We now state the convergence rate for the estimated velocity field obtained in (8).

Theorem 1 (Velocity field estimation). *Let $d \geq 3$. Suppose $\{t_k\}$ is time grid as follows*

$$\begin{aligned} 1 = t_0 > t_1 > \dots > t_{\mathbf{b}} = n^{-\frac{2}{2\alpha+d}} > \dots > t_{\mathbf{K}} = \\ \underline{\mathbf{t}} = n^{-\frac{\beta}{2\alpha+d}} \log^{\beta+1}(n), \quad 1 < \frac{t_k}{t_{k+1}} \leq 2 \end{aligned} \tag{11}$$

for $k = 0, 1, \dots, \mathbf{K}$. Let $\hat{v}(\mathbf{x}, t)$ be estimated velocity field obtained with the empirical optimization as in (8). Under the Assumptions 1, 2, and 3, we have:

A. for $n^{-\frac{\beta}{2\alpha+d}} \log^{\beta}(n) \leq \mathbf{t}_k < n^{-\frac{2}{2\alpha+d}}$,

$$\begin{aligned} & \mathbb{E}_{\mathcal{D}} \left[\int_{\mathbf{x}} \int_{t=1-t_k}^{1-t_{k+1}} \|\hat{v}(\mathbf{x}, t) - v_{\star}(\mathbf{x}, t)\|^2 \pi_t(x) dt d\mathbf{x} \right] \\ & \leq C \left(\frac{n^{-\frac{2\beta}{2\alpha+d}}}{t_k} + n^{-\frac{2\alpha}{2\alpha+d}} \cdot \log^{\alpha+1}(n) + \frac{\log^2(n)}{n} \right), \end{aligned}$$

where the neural network parameters satisfies

$$\begin{aligned} L_k &= \mathcal{O}\left(\log^4(n)\right), W_k = \mathcal{O}\left(n^{\frac{d}{2\alpha+d}} \log^{(6\vee 3+d)}(n)\right), \\ S_k &= \mathcal{O}\left(n^{\frac{d}{2\alpha+d}} \log^{(8\vee(5+d))}(n)\right), B_k = e^{\mathcal{O}(\log^4(n))}. \end{aligned}$$

B. for $n^{-\frac{2}{2\alpha+d}} \leq t_k < n^{-\frac{1}{6(2\alpha+d)}} \log^{-3}(n)$,

$$\begin{aligned} &\mathbb{E}_{\mathcal{D}} \left[\int_{\mathbf{x}} \int_{t=1-t_k}^{1-t_{k+1}} \|\widehat{v}(\mathbf{x}, t) - v_*(\mathbf{x}, t)\|^2 \pi_t(x) dt d\mathbf{x} \right] \\ &\leq C \left(\frac{\log^4(n)}{n} + \frac{t_k^{-d/2}}{n} \cdot \log^{14+d/2}(n) \right), \end{aligned}$$

where the neural network parameters satisfies

$$\begin{aligned} L_k &= \mathcal{O}(\log^4(n)), W_k = \mathcal{O}\left(t_k^{-d/2} \log^{(6\vee(d+3)-d/2)}(n)\right), \\ S_k &= \mathcal{O}\left(t_k^{-d/2} \log^{(8\vee(d+5)-d/2)}(n)\right), B_k = e^{\mathcal{O}(\log^4(n))}. \end{aligned}$$

C. for $n^{-\frac{1}{6(2\alpha+d)}} \log^{-3}(n) \leq t_k < 1$,

$$\begin{aligned} &\mathbb{E}_{\mathcal{D}} \left[\int_{\mathbf{x}} \int_{t=1-t_k}^{1-t_{k+1}} \|\widehat{v}(\mathbf{x}, t) - v_*(\mathbf{x}, t)\|^2 \pi_t(x) dt d\mathbf{x} \right] \\ &\leq C \left(\frac{\log^5(n)}{n} + n^{-\frac{(2\alpha+2)}{2\alpha+d}} \cdot \log^{2d+9}(n) \right), \end{aligned}$$

where the neural network parameters satisfies

$$\begin{aligned} L_k &= \mathcal{O}\left(\log^2(n)\right), W_k = \mathcal{O}\left(n^{\frac{d}{6(2\alpha+d)}} \log^{2d+3}(n)\right), \\ S_k &= \mathcal{O}\left(n^{\frac{d}{6(2\alpha+d)}} \log^{2d+4}(n)\right), B_k = e^{\mathcal{O}(\log^4(n))}. \end{aligned}$$

Here $C > 0$ is a constant depending on D , $C_{\mathcal{M}}$ and β .

The proof of Theorem 1 is provided in Section C.2. At a high level, the argument decomposes the estimation error into a bias term and a variance term. The bias is controlled via the neural-network approximation result in Corollary 1, while the variance is bounded using a uniform bound based on the covering numbers of the loss function class in Lemma 6. These ingredients are then combined through the M-estimation result in Lemma 12 to conclude the claim. As one can see, the rates are dependent on the intrinsic dimension d instead of the ambient dimension D .

Our results rely on a carefully designed fixed time grid that reflects the non-uniform difficulty of learning the velocity field in (4). In particular, the estimation problem becomes progressively harder as $t \rightarrow 1$, mirroring the singular behavior of $v^*(\cdot, t)$ near the terminal time. We therefore

Table 1: Comparison with existing theoretical results for flow matching.

	Key assumptions	Low-dimensional structure	Velocity field estimation	Optimality
Albergo and Vanden-Eijnden (2022)	$\mathbf{x} \mapsto \widehat{v}(\mathbf{x}, t)$ is \widehat{K} -Lipschitz	\times	\times	\times
Fukumizu et al. (2024)	Bounded support $\mathbf{x} \mapsto v^*(\mathbf{x}, t)$ is differentiable with $\ \nabla_{\mathbf{x}} v^*(\mathbf{x}, t)\ _{\text{op}} \lesssim \frac{1}{1-t}$	\times	\checkmark	\checkmark
Gao et al. (2024b)	$\mathbf{x} \mapsto v^*(\mathbf{x}, t)$ is L -Lipschitz with $L \lesssim 1$	\times	\checkmark	\times
Zhou and Liu (2025)	Bounded support $\mathbf{x} \mapsto v^*(\mathbf{x}, t)$ is L -Lipschitz with $L \lesssim 1$	\times	\checkmark	\times
Kunkel and Trabs (2025)	Bounded support $\mathbf{x} \mapsto v^*(\mathbf{x}, t)$ is Lipschitz continuous	\checkmark (linear subspace)	\checkmark (overparametrized network)	\checkmark
Ours	Bounded support $\ \nabla_{\mathbf{x}} v^*(\mathbf{x}, t)\ _{\text{op}} \lesssim \frac{1}{(1-t)^{1-\xi}}$ $\xi \approx (\log \log(n))^{-1}$	\checkmark (manifold)	\checkmark	\checkmark

refine the grid close to $t = 1$ and employ early stopping at $t = 1 - \mathfrak{t}$ to avoid the endpoint singularity. On each intermediate time slab, the appropriate network architecture, and the resulting estimation rate, depends on the local temporal resolution, quantified by the time grid width $t_k - t_{k+1} = \mathcal{O}(t_k)$. By contrast, at times away from from $t = 1$, the estimation error is essentially insensitive to t_k , and the network parameters can be chosen as a function of n alone. Extending the analysis to random time-grid designs, which are commonly used in practice (Lipman et al., 2022), would substantially complicate the proof structure; we therefore leave a systematic treatment of such grids to future work.

Theorem 2 (Main result). *Let $d \geq 3$. Suppose $\widehat{\pi}_{1-\mathfrak{t}}$ denotes the density of $\widehat{X}_{1-\mathfrak{t}}$ as in (10). Under the Assumptions 1, 2, and 3 setup of Theorem 1, assume $1 > \xi \geq C_{\text{Lip}} / \log \log(n)$. Then*

$$\mathbb{E}_{\mathcal{D}} \left[W_2 \left(\widehat{\pi}_{1-\mathfrak{t}}, \pi_1 \right) \right] \leq C \left(n^{-\frac{\beta}{2\alpha+d}} \log^{\beta V^2}(n) + n^{-\frac{\alpha+1}{2\alpha+d}} \log^{d+9}(n) + n^{-1/2} \log^4(n) \right),$$

where $C > 0$ is a constant independent of n (depending only on D , $C_{\mathcal{M}}$, and β).

The proof of Theorem 2 is provided in Section A. It is based on the error decomposition in Lemma 4, which separates (i) the early-stopping error and (ii) an accumulated estimation error obtained by summing the velocity-field estimation error over the time-grid, weighted by the corresponding grid lengths. The early-stopping term is bounded in Lemma 3, while the accumulated estimation term is controlled using Theorem 1.

Theorem 2 shows that flow matching with linear interpolation adapts to the (unknown) manifold structure underlying the data. The resulting convergence rate, up to log factors, decomposes into three terms, $n^{-\beta/(2\alpha+d)}$, $n^{-(\alpha+1)/(2\alpha+d)}$, and $n^{-1/2}$. The second term matches the classical rate for density estimation on a d -dimensional manifold, whereas the first term captures an additional contribution that couples support (manifold) estimation with density estimation. In contrast, the minimax lower bound for this problem is $n^{-\beta/d} + n^{-(\alpha+1)/(2\alpha+d)} + n^{-1/2}$ (Tang and Yang,

2023, Theorem 1). The first component corresponds to pure manifold recovery, while the second corresponds to density estimation given the manifold.

Our upper bound is therefore near-optimal: it recovers the density-estimation term exactly, and it is minimax optimal in regimes where this term dominates the overall error. The remaining gap lies in the support-estimation component: $n^{-\beta/(2\alpha+d)}$ is slower than the optimal manifold-estimation rate $n^{-\beta/d}$ (Aamari and Levrard, 2019; Divol, 2022). We conjecture that this discrepancy is driven by the interpolation-based training objective, which introduces additional statistical difficulty in the near-terminal (singular) time regime; related methods such as diffusion diffusion display similar rate degradations (Azangulov et al., 2024; Tang and Yang, 2024).

We compare our work with prior results on flow matching in Table 1. A key distinction is the regularity imposed on the velocity field v^* . In particular, the assumption that $x \mapsto v^*(x, t)$ is L -Lipschitz with $L \lesssim 1$ is quite restrictive, as it effectively narrows the admissible class of target distributions. For instance, the analysis of Gao et al. (2024b) applies primarily to log-concave π_1 and closely related families, including certain near-Gaussian variants. Although Kunkel and Trabs (2025) remove the global Lipschitz requirement, their guarantees still rely on a vanilla KDE that adapts to the target ambient-space density. This assumption breaks down when π_1 is singular and is supported on an unknown low-dimensional manifold (Ozakin and Gray, 2009).

4 Numerical results

We present numerical experiments across three synthetic data settings to validate the theoretical results on the manifold adaptivity of flow matching. In all cases the target law π_1 is supported on a smooth, low-dimensional manifold $\mathcal{M} \subset \mathbb{R}^D$ with intrinsic dimension $d \ll D$, while the source π_0 is a standard Gaussian on \mathbb{R}^D .

4.1 Example target distributions

We present numerical results of flow matching on the following three example target distributions.

Example 1 (Sphere embedded in high dimension). *Fix an intrinsic dimension $d \geq 2$ and define the manifold*

$$\mathcal{M} = \mathbb{S}^d \times \{0\}^{D-(d+1)} \subset \mathbb{R}^D,$$

i.e., the unit d -sphere embedded in the first $d+1$ coordinates and padded with zeros in the remaining coordinates.

Target distribution π_1 . *We use a smooth, non-uniform distribution on the sphere via a projected Gaussian Sample*

$$Z \sim \mathcal{N}(\gamma, \mathbb{I}_{d+1}), \quad Y := \frac{Z}{\|Z\|_2} \in \mathbb{S}^d,$$

and finally embed into \mathbb{R}^D by padding $X_1 := (Y, 0, \dots, 0) \in \mathbb{R}^D$.

Example 2 (Rotated d -torus embedded in \mathbb{R}^D). *Define the axis-aligned d -torus embedding in \mathbb{R}^D by*

$$\mathcal{M}_0 = \left\{ (\cos \theta_1, \sin \theta_1, \dots, \cos \theta_d, \sin \theta_d, 0, \dots, 0) \in \mathbb{R}^D \right\},$$

where $\boldsymbol{\theta} \in \mathbb{R}^d$, and $\boldsymbol{\theta}_i = \boldsymbol{\phi} + \gamma_1 \cdot i + \epsilon_i$. Here

$$\boldsymbol{\phi} \sim \text{Unif}\{-1, 1\} \quad \text{and} \quad \epsilon_i = \mathbb{N}(-\gamma_1, \sigma_1^2).$$

To remove axis alignment, let $\mathbf{O} \in \mathbb{O}_D$ be an arbitrary orthogonal matrix. We define the rotated torus as

$$\mathcal{M} = \left\{ \mathbf{x}_0(\boldsymbol{\theta}) \cdot \mathbf{O}^\top : \mathbf{x}_0(\boldsymbol{\theta}) \in \mathcal{M}_0 \right\}.$$

Example 3 (Floral segments embedded in \mathbb{R}^D). Fix $d = 1$ and $D = 2$, and let $m \geq 2$ denote the number of petals. For each $i \in \{0, 1, \dots, m-1\}$, define a spiral-segment curve

$$\psi_i(t) = \left(r(t) \cos \theta_i(t), r(t) \sin \theta_i(t) \right) \in \mathbb{R}^2, \quad t \in [0, 1],$$

where the radius increases linearly and the angle rotates slightly along the segment:

$$r(t) = r_{\text{in}} + t(r_{\text{out}} - r_{\text{in}}), \quad \theta_i(t) = \frac{2\pi i}{m} + 2\pi \tau t.$$

Here $0 < r_{\text{in}} < r_{\text{out}}$ control the inner and outer radii, and $\tau \in (0, 1)$ determines the angular twist of each petal.

We define the manifold as the union of these spiral segments,

$$\mathcal{M}_0 = \bigcup_{i=0}^{m-1} \{ \psi_i(t) : t \in [0, 1] \} \subset \mathbb{R}^2.$$

Target distribution π_1 . Draw $i \sim \text{Unif}\{0, \dots, m-1\}$ and $t \sim \text{Unif}[0, 1]$, independently. Let $Z_1, Z_2, Z_3 \sim \mathbb{N}(0, 1)$ be independent noises. Define $\theta'_i = \theta_i(t) + \sigma_\theta Z_1$, and generate the observed point in \mathbb{R}^2 by

$$X = \left(r(t) \cos(\theta'_i), r(t) \sin(\theta'_i) \right) + \sigma_r \cdot (Z_2, Z_3).$$

4.2 Implementation details

- **Sphere.** We set the parameter values $\gamma = \mathbf{0}_{d+1}$ and consider intrinsic dimensions $d \in \{2, 3, 4, 5\}$. The ambient dimension chosen as $D \in \{2d, 3d, 4d\}$ for each d . The velocity field v is parametrized by a multilayer perceptron network with width 256 and depth 4, ReLU activations, and a linear output layer of dimension D . Training is performed using AdamW with learning rate 2×10^{-4} , batch size 2048, and 1,000 iterations. For generation, we solve the learned ODE with forward Euler using $N = 250$ steps on the nonuniform grid $t_i = 1 - (1 - i/N)^2$, $i = 0, \dots, N$.
- **Torus.** In this experiment, we use the parameter values $\gamma_1 = 0.35$ and $\sigma_1^2 = 0.35^2 + 0.15^2$. The choice of (d, D) is the same as in the previous case. All other training settings remain unchanged, except that the network depth is increased to 6 instead of 4.
- **Floral segments.** We use the parameter values

$$(m, r_{\text{in}}, r_{\text{out}}, \tau, \sigma_r, \sigma_\theta) = (5, 1, 4, 0.2, 0.05, 0.05).$$

The velocity field v is parametrized by a multilayer perceptron conditioned on t via a sinusoidal time embedding. We use a fully-connected network with width 256 and depth 4, ReLU activations, and a linear output layer in \mathbb{R}^2 . Training is performed using Adam with learning rate 10^{-3} , batch size 512, and 5,000 iterations. A cosine annealing learning-rate schedule is applied with $T_{\text{max}} = 5000$ steps. For generation, we solve the ODE using the fourth-order Runge-Kutta with $N = 500$ time steps, using the discretization $t_i = [1 - (1 - i/N)^2]$, $i = 0, \dots, N$.

4.3 Evaluations

We evaluate the quality of the generated samples in Examples 1 and 2 using two complementary metrics: (i) the sliced Wasserstein distance (Karras et al., 2018; Kolouri et al., 2019), which measures distributional discrepancy, and (ii) the distance to the manifold, which quantifies geometric fidelity. Specifically, we report the standardized empirical sliced Wasserstein distance ($W_{1,\text{slice}}^{\text{std}}$) and an empirical estimate of the manifold distance ($\text{dist}_{\mathcal{M}}$).

For each (d, D) , we repeat evaluation over $R = 5$ independent runs and report mean and standard deviation Tables 2 and 3. Across both the sphere and torus families, $W_{1,\text{slice}}^{\text{std}}$ remains of the same order across ambient dimensions, while $\text{dist}_{\mathcal{M}}$ stays small, indicating that the learned flow.

Table 2: Mean and standard deviation of $W_{1,\text{slice}}^{\text{std}}$ and $\text{dist}_{\mathcal{M}}$ for estimated density in Example 1 across (d, D) .

d	D	$W_{1,\text{slice}}^{\text{std}}$	$\text{dist}_{\mathcal{M}}$
2	4	0.04177 ± 0.01935	0.05304 ± 0.00460
	6	0.03788 ± 0.00725	0.05920 ± 0.00339
	8	0.04194 ± 0.01330	0.05861 ± 0.00589
3	6	0.03277 ± 0.00573	0.07028 ± 0.00140
	9	0.03994 ± 0.00997	0.06962 ± 0.00622
	12	0.04648 ± 0.01795	0.07906 ± 0.00353
4	8	0.03084 ± 0.00732	0.07861 ± 0.00261
	12	0.04097 ± 0.00590	0.07979 ± 0.00180
	16	0.05370 ± 0.01152	0.10544 ± 0.00294
5	10	0.03768 ± 0.00901	0.08246 ± 0.00226
	15	0.04473 ± 0.00780	0.10290 ± 0.00450
	20	0.05324 ± 0.00657	0.14034 ± 0.00131

Example 3 is supported on a union of low-dimensional manifolds, making it a useful visual stress-test. We therefore provide samples in Figure 1, which show that the learned sampler reproduces the multi-petal structure and generates points that lie on the spiral segments.

5 Discussion

We study the theoretical properties of flow matching with the linear interpolation path when the target distribution is supported on a low-dimensional manifold. We show that the convergence rate of the resulting implicit density estimator is governed by the manifold’s intrinsic dimension (rather than the ambient dimension). These results lay statistical foundations of flow-matching based models by providing a principled explanation for why linear-path flow matching can mitigate the curse of dimensionality by adapting to the intrinsic geometry of the data.

Future work. There are several interesting future directions to pursue: (i) Extend our theory to the more realistic setting where data are concentrated near a low-dimensional manifold. For

Table 3: Mean and standard deviation of $W_{1,\text{slice}}^{\text{std}}$ and $\text{dist}_{\mathcal{M}}$ for estimated density in Example 2 across (d, D) .

d	D	$W_{1,\text{slice}}^{\text{std}}$	$\text{dist}_{\mathcal{M}}$
2	4	0.04407 ± 0.01421	0.05022 ± 0.00291
	6	0.02430 ± 0.00407	0.06331 ± 0.00212
	8	0.03548 ± 0.01123	0.07248 ± 0.00218
3	6	0.02998 ± 0.01201	0.07268 ± 0.00218
	9	0.03790 ± 0.01672	0.09524 ± 0.00215
	12	0.03792 ± 0.00951	0.11211 ± 0.00311
4	8	0.02833 ± 0.01532	0.10091 ± 0.00330
	12	0.02788 ± 0.00577	0.13726 ± 0.00369
	16	0.03859 ± 0.01159	0.17358 ± 0.00611
5	10	0.03017 ± 0.01236	0.13094 ± 0.00347
	15	0.03492 ± 0.00572	0.18492 ± 0.00265
	20	0.04205 ± 0.01155	0.23003 ± 0.00515

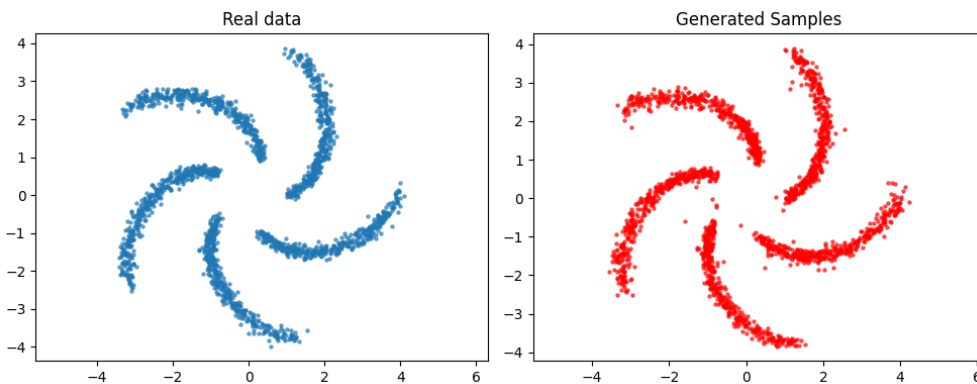


Figure 1: Comparison of generated samples and training data for Example 3. The learned flow generates samples that recover the petal geometry and place negligible mass in the regions between segments.

instance, when observations are corrupted by small, decaying noise around a manifold-supported distribution. In this regime, we expect the early-stopping requirement may be removable and the regularity of the velocity field may improve, since the singular behavior near $t = 1$ should be smoothed out. (ii) Investigate stratified settings in which the target distribution lies on a union of disjoint manifolds, as suggested by the floral example. It would be interesting to characterize the resulting regularity properties and to derive estimation rates for both the velocity field and the induced implicit density estimator, and (iii) another interesting direction is to employ flow based models for conditional distribution estimation or distribution regression where one incorporates additional covariates or control information in modeling the underlying distribution.

References

- Aamari, E. and Levrard, C. (2019). Nonasymptotic rates for manifold, tangent space and curvature estimation. *The Annals of Statistics*, 47(1):177 – 204.
- Albergo, M. S., Boffi, N. M., and Vanden-Eijnden, E. (2023). Stochastic interpolants: A unifying framework for flows and diffusions. *arXiv preprint arXiv:2303.08797*.
- Albergo, M. S. and Vanden-Eijnden, E. (2022). Building normalizing flows with stochastic interpolants. *arXiv preprint arXiv:2209.15571*.
- Azangulov, I., Deligiannidis, G., and Rousseau, J. (2024). Convergence of diffusion models under the manifold hypothesis in high-dimensions. *arXiv preprint arXiv:2409.18804*.
- Bansal, V., Roy, S., Sarkar, P., and Rinaldo, A. (2024). On the wasserstein convergence and straightness of rectified flow. *arXiv preprint arXiv:2410.14949*.
- Bose, A. J., Akhound-Sadegh, T., Huguet, G., Fatras, K., Rector-Brooks, J., Liu, C.-H., Nica, A. C., Korablyov, M., Bronstein, M., and Tong, A. (2023). Se (3)-stochastic flow matching for protein backbone generation. *arXiv preprint arXiv:2310.02391*.
- Chen, R. T. and Lipman, Y. (2023). Flow matching on general geometries. *arXiv preprint arXiv:2302.03660*.
- Cheng, C., Li, J., Fan, J., and Liu, G. (2025). α -flow: A unified framework for continuous-state discrete flow matching models. *arXiv preprint arXiv:2504.10283*.
- Coddington, E. A. and Levinson, N. (1955). *Theory of Ordinary Differential Equations*. McGraw-Hill.
- Dao, Q., Phung, H., Nguyen, B., and Tran, A. (2023). Flow matching in latent space. *arXiv preprint arXiv:2307.08698*.
- Davis, O., Kessler, S., Petrache, M., Ceylan, İ. İ., Bronstein, M., and Bose, A. J. (2024). Fisher flow matching for generative modeling over discrete data. *Advances in Neural Information Processing Systems*, 37:139054–139084.
- Divol, V. (2022). Measure estimation on manifolds: an optimal transport approach. *Probability Theory and Related Fields*, 183(1):581–647.
- Esser, P., Kulal, S., Blattmann, A., Entezari, R., Müller, J., Saini, H., Levi, Y., Lorenz, D., Sauer, A., Boesel, F., et al. (2024). Scaling rectified flow transformers for high-resolution image synthesis. In *Forty-first international conference on machine learning*.
- Fukumizu, K., Suzuki, T., Isobe, N., Oko, K., and Koyama, M. (2024). Flow matching achieves almost minimax optimal convergence. *arXiv preprint arXiv:2405.20879*.
- Gao, Y., Huang, J., and Jiao, Y. (2024a). Gaussian interpolation flows. *Journal of Machine Learning Research*, 25(253):1–52.
- Gao, Y., Huang, J., Jiao, Y., and Zheng, S. (2024b). Convergence of continuous normalizing flows for learning probability distributions. *arXiv preprint arXiv:2404.00551*.

- Gat, I., Remez, T., Shaul, N., Kreuk, F., Chen, R. T., Synnaeve, G., Adi, Y., and Lipman, Y. (2024). Discrete flow matching. *Advances in Neural Information Processing Systems*, 37:133345–133385.
- Graham, Y. and Purver, M. (2024). Proceedings of the 18th conference of the european chapter of the association for computational linguistics (volume 1: Long papers). In *Proceedings of the 18th Conference of the European Chapter of the Association for Computational Linguistics (Volume 1: Long Papers)*.
- Gui, M., Schusterbauer, J., Prestel, U., Ma, P., Kotovenko, D., Grebenkova, O., Baumann, S. A., Hu, V. T., and Ommer, B. (2025). Depthfm: Fast generative monocular depth estimation with flow matching. In *Proceedings of the AAAI Conference on Artificial Intelligence*, volume 39, pages 3203–3211.
- Hu, V., Wu, D., Asano, Y., Mettes, P., Fernando, B., Ommer, B., and Snoek, C. (2024a). Flow matching for conditional text generation in a few sampling steps. In *Proceedings of the 18th Conference of the European Chapter of the Association for Computational Linguistics (Volume 2: Short Papers)*, pages 380–392.
- Hu, V. T., Zhang, W., Tang, M., Mettes, P., Zhao, D., and Snoek, C. (2024b). Latent space editing in transformer-based flow matching. In *Proceedings of the AAAI conference on artificial intelligence*, volume 38, pages 2247–2255.
- Karras, T., Aila, T., Laine, S., and Lehtinen, J. (2018). Progressive growing of GANs for improved quality, stability, and variation. In *International Conference on Learning Representations (ICLR)*.
- Kolouri, S., Nadjahi, K., Simsekli, U., Badeau, R., and Rohde, G. (2019). Generalized sliced wasserstein distances. *Advances in neural information processing systems*, 32.
- Kornilov, N., Mokrov, P., Gasnikov, A., and Korotin, A. (2024). Optimal flow matching: Learning straight trajectories in just one step. *Advances in Neural Information Processing Systems*, 37:104180–104204.
- Kunkel, L. (2025a). Distribution estimation via flow matching with lipschitz guarantees. *arXiv preprint arXiv:2509.02337*.
- Kunkel, L. and Trabs, M. (2025). On the minimax optimality of flow matching through the connection to kernel density estimation. *arXiv preprint arXiv:2504.13336*.
- Kunkel, L. M. (2025b). *Statistical Guarantees for Generative Models as Distribution Estimators*. PhD thesis, Karlsruher Institut für Technologie (KIT).
- Lipman, Y., Chen, R. T., Ben-Hamu, H., Nickel, M., and Le, M. (2022). Flow matching for generative modeling. *arXiv preprint arXiv:2210.02747*.
- Liu, X., Gong, C., and Liu, Q. (2022). Flow straight and fast: Learning to generate and transfer data with rectified flow. *arXiv preprint arXiv:2209.03003*.

- Ma, N., Goldstein, M., Albergo, M. S., Boffi, N. M., Vanden-Eijnden, E., and Xie, S. (2024). Sit: Exploring flow and diffusion-based generative models with scalable interpolant transformers. In *European Conference on Computer Vision*, pages 23–40. Springer.
- Marzouk, Y., Ren, Z. R., Wang, S., and Zech, J. (2024). Distribution learning via neural differential equations: a nonparametric statistical perspective. *Journal of Machine Learning Research*, 25(232):1–61.
- Ozakin, A. and Gray, A. (2009). Submanifold density estimation. *Advances in neural information processing systems*, 22.
- Su, M., Lu, M., Hu, J. Y.-C., Wu, S., Song, Z., Reneau, A., and Liu, H. (2025). A theoretical analysis of discrete flow matching generative models. *arXiv preprint arXiv:2509.22623*.
- Tang, R. and Yang, Y. (2023). Minimax rate of distribution estimation on unknown submanifolds under adversarial losses. *The Annals of Statistics*, 51(3):1282 – 1308.
- Tang, R. and Yang, Y. (2024). Adaptivity of diffusion models to manifold structures. In *International Conference on Artificial Intelligence and Statistics*, pages 1648–1656. PMLR.
- Tong, A., Fatras, K., Malkin, N., Huguet, G., Zhang, Y., Rector-Brooks, J., Wolf, G., and Bengio, Y. (2023). Improving and generalizing flow-based generative models with minibatch optimal transport. *arXiv preprint arXiv:2302.00482*.
- Zhou, Z. and Liu, W. (2025). An error analysis of flow matching for deep generative modeling. In *Proceedings of the 42nd International Conference on Machine Learning*, volume 267 of *Proceedings of Machine Learning Research*, pages 78903–78932. PMLR.